nature geoscience

ARTICLES

https://doi.org/10.1038/s41561-020-00656-2

Increased typhoon activity in the Pacific deep tropics driven by Little Ice Age circulation changes

James F. Bramante[1,2]✉, Murray R. Ford[3], Paul S. Kench[4], Andrew D. Ashton[1], Michael R. Toomey[5], Richard M. Sullivan[1], Kristopher B. Karnauskas[6], Caroline C. Ummenhofer[7] and Jeffrey P. Donnelly[1]

The instrumental record reveals that tropical cyclone activity is sensitive to oceanic and atmospheric variability on inter-annual and decadal scales. However, our understanding of the influence of climate on tropical cyclone behaviour is restricted by the short historical record and the sparseness of prehistorical reconstructions, particularly in the western North Pacific, where coastal communities suffer loss of life and livelihood from typhoons annually. Here, to explore past regional typhoon dynamics, we reconstruct three millennia of deep tropical North Pacific cyclogenesis. Combined with existing records, our reconstruction demonstrates that low-baseline typhoon activity prior to 1350 CE was followed by an interval of frequent storms during the Little Ice Age. This pattern, concurrent with hydroclimate proxy variability, suggests a centennial-scale link between Pacific hydroclimate and tropical cyclone climatology. An ensemble of global climate models demonstrates a migration of the Pacific Walker circulation and variability in two Pacific climate modes during the Little Ice Age, which probably contributed to enhanced tropical cyclone activity in the tropical western North Pacific. In the next century, projected changes to the Pacific Walker circulation and expansion of the tropics will invert these Little Ice Age hydroclimate trends, potentially reducing typhoon activity in the deep tropical Pacific.

Determining the hazard risk of coastal communities owing to climate change requires an understanding of the influence of climate variability on tropical cyclone (TC) activity. From 2010 to 2030, global population growth is estimated to increase the number of people exposed annually to TCs from 133.7 million to 149.3 million, 90% of whom live along the Asian Pacific coastline[1]. Simultaneously, anthropogenic forcing is expected to alter global climate, affecting the frequency, geographic distribution and intensity of TCs[2,3]. However, the influence of global climate is mediated by regional climate characteristics, which vary on seasonal to centennial timescales[4–8]. Understanding the mechanisms by which TCs have varied in response to past forcing will help us understand how TC risk might change with continued anthropogenic radiative forcing.

Our understanding of climate controls on TCs is limited by the observational record. The western North Pacific (WNP) is the most active basin for TCs globally; however, few pre-modern reconstructions with annual to decadal resolution have been developed for this region[9–11] relative to the western North Atlantic[6,12–16]. This dearth of WNP TC reconstructions hinders identification of the internal and external processes that drive low-frequency variability in TC statistics. As TCs travel, they are influenced by variable environmental conditions along their tracks[2]. Separating the effects of different aggregate TC characteristics (that is, genesis frequency, genesis location, storm track and landfall intensity) on the reconstructed variability is difficult when a reconstruction is located far from the genesis locations. In the western North Atlantic, recent research has overcome this difficulty by contrasting records at many sites across the basin, revealing that regional ocean circulation likely altered the dominant storm track, in turn driving a cross-basin shift in TC landfall frequency from the Gulf of Mexico to the northeastern United States around 550 cal yr BP[6,12]. In the WNP, however, the few TC reconstructions that exist are located far from the primary cyclogenesis regions. Thus, attempts to contrast records on the western basin margin have failed to identify the TC characteristics and drivers responsible for a clear southward shift in landfall frequency 500 cal yr BP[9,17], for example.

Here, we introduce a sediment proxy reconstruction of TC landfall frequency that captures genesis variability in the deep tropical central Pacific—a hotspot of tropical cyclogenesis that feeds the WNP basin. Tropical cyclogenesis potential in the WNP is expected to increase with the rise in sea surface temperatures (SSTs) and weakening of vertical wind shear (VWS) projected over the twenty-first century[18]. The proximity between the genesis location and the proxy site mitigates the influence of the storm track and post-genesis intensification on our reconstruction. By focusing on TC genesis and using a multi-model ensemble of general circulation models (GCMs), we can identify the climate patterns influencing cyclogenesis variability near our site.

Tropical cyclone genesis over the past 3,000 years

We developed a grain-size proxy of cross-reef sediment transport intensity from a sediment core retrieved from a blue hole, a 30-m-deep karst basin, on Jaluit Atoll (6.256° N, 169.411° E, Extended Data Fig. 1). Coastal basins preserve evidence of the close passage of intense TCs as anomalously coarse layers of sediment[13,15]. We sieved the core sediment and identified TC deposits as peaks in the sediment coarse fraction (250–2,000 μm sieve diameter) that exceeded a statistical threshold (see Methods). A post-bomb radiocarbon date indicates that the youngest coarse layer was deposited

[1]Department of Geology and Geophysics, Woods Hole Oceanographic Institution, Woods Hole, MA, USA. [2]Department of Earth, Atmospheric, and Planetary Sciences, Massachusetts Institute of Technology, Cambridge, MA, USA. [3]School of Environment, The University of Auckland, Auckland, New Zealand. [4]Department of Earth Sciences, Simon Fraser University, Burnaby, British Columbia, Canada. [5]US Geological Survey, Florence Bascom Geoscience Center, Reston, VA, USA. [6]Department of Atmospheric and Ocean Sciences, University of Colorado, Boulder, CO, USA. [7]Department of Physical Oceanography, Woods Hole Oceanographic Institution, Woods Hole, MA, USA. ✉e-mail: james.f.bramante@gmail.com

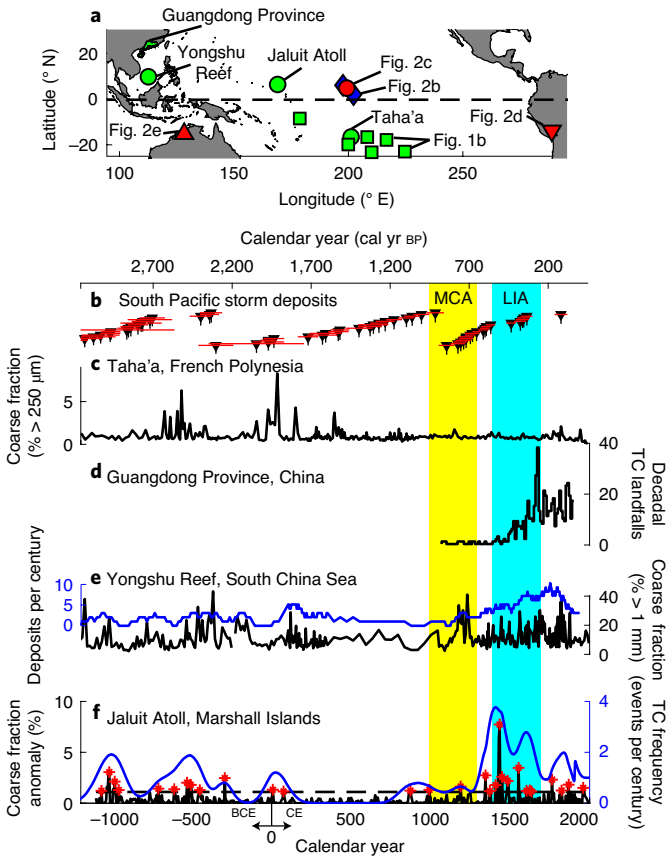

Fig. 1 | Western Pacific tropical cyclone reconstructions. a, Location of records in Figs. 1 and 2; symbol definitions can be found in Extended Data Fig. 1. **b**, Radiocarbon dates (±1 standard deviation) from South Pacific storm-deposited boulders[21,22]. **c**, Storm deposits in a back-barrier reef lagoon, Taha'a, French Polynesia[20]. **d**, TC landfalls in Guangdong Province and imperial Chinese historical records[10]. **e**, Coarse fraction (black line) and centennial frequency (blue line) of large wave deposits at Yongshu Reef[11]. **f**, Coarse fraction (250–2,000 µm) anomaly (black line) from Jaluit Atoll and centennial frequency (blue line) of identified storm deposits (red asterisks) (this study). The error in **c**, **e** and **f** is less than ±0.05%, which is too small for plotting. Uncertainty estimates were unavailable for **d**.

in the late 1950s and probably by Typhoon Ophelia in 1958, which passed directly over Jaluit with estimated sustained winds of over 64 m s^{-1} (nearly a super typhoon, or Category 4 on the Saffir–Simpson scale), causing widespread destruction[19]. The coarse fraction anomalies of all identified event beds are close to or exceed that of Ophelia, suggesting that the frequency of coarse deposits in our core corresponds to the frequency of intense TC passage near Jaluit over the past 3,000 years. Owing to the position of the site southeast of the WNP basin, near the geographical limits of the observed tropical cyclogenesis, we interpret temporal variability in our record as directly corresponding to temporal variability in nearby cyclogenesis (see Supplementary Discussion).

Our reconstruction of centennial TC frequency shows a mean of 1 event per century and centennial variability similar to other reconstructions from the western Pacific. The most prominent feature in our record is a peak in frequency c. 1350–1700 CE with a maximum of 3.75 events per century that encompasses the early Little Ice Age (LIA, 1400–1700 CE), which is higher than that during any other period (Fig. 1e) and is unlikely to be the product of unforced variability (Methods). Immediately preceding the LIA peak was a relatively quiet interval encompassing the Medieval Climate Anomaly (MCA, 1000–1300 CE). The LIA peak in cyclogenesis at Jaluit is synchronous with a substantial increase in the frequency of coarse deposits at Yongshu Reef in a South China Sea (SCS) sediment core, indicating enhanced landfall frequency relative to the MCA[11] and enhanced landfall frequency in Guangdong Province according to Chinese historical records[10] (Fig. 1c,d). A sedimentary reconstruction of TC landfall on Taha'a, French Polynesia, recorded few storms over the past 1,000 years[20], but reef-top storm deposits collected from across the central South Pacific basin suggest higher TC activity during the MCA than during the LIA[21,22] (Fig. 1a,b).

Large-scale drivers of tropical cyclone variability

In the instrumental record, the El Niño Southern Oscillation (ENSO) dominates inter-annual variability in western Pacific cyclogenesis. During El Niño events, the mean TC genesis location in the WNP shifts to the southeast, and TCs tend to recurve north more than in non-event years[23,24]. Thus, El Niño events result in more frequent cyclogenesis near Jaluit but fewer storm tracks crossing the SCS near Yongshu Reef[24]. In the South Pacific, El Niño events tend to shift the mean genesis location eastward, resulting in fewer cyclone landfalls in Australia but more in the central South Pacific and French Polynesia[21,25]. These effects scale with the intensity of ENSO-associated SST anomalies and are more sensitive to central Pacific warming than eastern Pacific El Niño events[24].

Given the dominant influence of ENSO on cyclogenesis in the WNP historically, variations in ENSO over the past few millennia could have contributed to the variability in our reconstruction. A synthesis of annually resolved SST proxies for the Niño 3.4 region[26] demonstrates that SST variability associated with ENSO was lower over much of the last millennium relative to the last century (Fig. 2a). However, over this background signal, there were two century-long periods of elevated ENSO variability that correspond with the beginning and end of the active interval in our record. Additionally, an annually resolved reconstruction of SSTs in the Niño 4 region from Taiwanese tree-ring $\delta^{18}O$ reveals a peak in ENSO-associated variability c. 1350–1425 CE, during peak cyclogenesis in our reconstruction[27]. Coral-based SST proxies from the central Pacific detail similar but shorter-duration fluctuations in ENSO variability during the LIA[28] (Fig. 2b). These transient peaks in ENSO-associated SST variability imply more frequent or more intense El Niño events, either of which would have increased the frequency of TC cyclogenesis near Jaluit and thus likely increased the frequency of TCs in our record.

However, the SST reconstructions also indicate that ENSO-associated variability was higher during the last century than during the LIA, contrary to cyclogenesis in our reconstruction. Additionally, the enhanced frequency or magnitude of El Niño events suggested by peaks in ENSO-associated variability cannot explain enhanced landfall frequency near Yongshu Reef and the absence of an increase in TC activity in the central South Pacific during the LIA. Thus, it is likely that other factors contributed substantially to cyclogenesis variability over the last millennium.

Hydroclimate proxies from the Indo-Pacific Warm Pool (IPWP) and the central and eastern Pacific demonstrate rapid, synchronous and spatially consistent change at the onset of the LIA. Around 1400 CE, $\delta^{18}O$ records from speleothems in northwestern Australia and southern China demonstrate a rapid transition to a drier climate that lasted until c. 1750 CE[29] (Fig. 2e). Simultaneously, precipitation proxies in the deep tropical IPWP and SCS indicate the rapid onset of a wetter climate[30,31]. These shifts have been attributed to a contraction of the Intertropical Convergence Zone (ITCZ)[29,31] (Fig. 2e) and a westward shift in the Pacific Walker circulation (PWC)[30]. Simultaneously, an algal lipid δD record indicates a rapid onset of dry conditions in the central North Pacific[32] (Fig. 2c), and enhanced ice accumulation in Quelccaya ice cap, Peru[33] (Fig. 2d) indicates wetter conditions in the eastern South Pacific. These

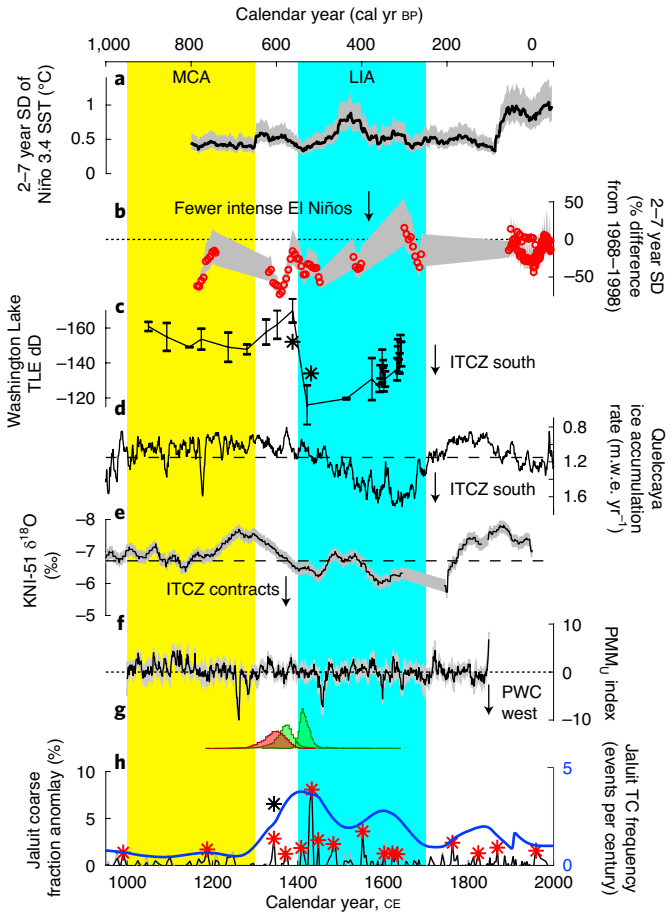

Fig. 2 | Comparison of our storm reconstruction with Pacific paleoclimate proxies. a, ENSO-band standard deviation (SD) calculated in a 31-year moving window of a multi-proxy reconstruction of Niño 3.4 region SST anomalies[26]. **b**, Normalized ENSO-band SD of SSTs from coral $\delta^{18}O$ proxies[28,50]. **c**, Lipid δD proxy of precipitation from Washington Lake, Washington Island, Northern Line Islands[32]. **d**, Ice accumulation rates in metres water equivalent (m.w.e.) in a core from the Quelccaya ice cap, Peru[33]. **e**, Speleothem $\delta^{18}O$ proxy of precipitation from cave KNI-51, northwestern Australia[29]. **f**, CMIP5 ensemble median (black line) ± standard error (grey shading) of decadally averaged PMM wind index anomaly (this study). **g**, Comparison of age model histograms from samples indicated by black asterisks in **c** and **h**. **h**, same as Fig. 1f. The dashed black lines indicate 1000–1850 CE means and the dotted black lines indicate zero values. The grey shading in **a**, **b** and **e** indicate 95% confidence intervals. Uncertainty estimates unavailable for **d**.

meridional shifts in precipitation have been attributed to a southward displacement of the ITCZ during the LIA. A radiocarbon date from 5 cm above the first event layer in the LIA active interval constrains its modelled age distribution to overlap with the onset of these changes in hydroclimate proxies in the Pacific (Fig. 2g). Thus, the start of the LIA active interval may have been concurrent with the basin-wide transitions between wet and dry conditions.

The tropical atmospheric circulation patterns driving hydroclimate variability during the LIA could have influenced cyclogenesis across the western Pacific. Contraction of the ITCZ would entail contraction in the Hadley circulation, which influences the characteristics (latitude, width, intensity) of zonal mean precipitation in the tropics. Recent research suggests tropical cyclogenesis in the WNP shifted to the north over the past few decades as the Hadley cell expanded poleward owing to anthropogenic climate change[34,35]. Assuming Hadley cell contraction would have the opposite effect, the LIA contraction could have enhanced cyclogenesis in the deep tropics (0–10° N) near Jaluit. Alternatively, inter-annual variability in the Pacific Meridional Mode (PMM) has influenced PWC and correlated with zonal shifts in WNP cyclogenesis over the past few decades[7,36]. Thus, westward migration of the rising limb of the PWC could have shifted cyclogenesis westward during the LIA as well.

Detection of climatic drivers in a climate model ensemble

To explore the associations between tropical atmospheric circulation and temporal variability in our reconstruction, we analysed the results of the Last Millennium experiment in an ensemble of Coupled Model Intercomparison Project Phase 5 (CMIP5) GCMs. By diagnosing the genesis potential index (GPI)[37,38] from the monthly mean climate model output, we determined that the ensemble predicted cyclogenesis anomalies during the LIA relative to the MCA that were consistent with TC reconstructions across the tropical WNP (Fig. 3a). The ensemble indicated anomalously high GPI in the vicinity of the Philippines. Assuming TCs entering the SCS are generated primarily to the east and southeast, these results are consistent with the Yongshu Reef proxy reconstruction[11] and historical records from Guangdong[10], both of which recorded enhanced TC activity during the LIA relative to the MCA (Fig. 1d). In the near-equatorial central North Pacific, where most TCs recorded at Jaluit originate, the ensemble showed patchy positive GPI anomalies, while the GPI was reduced directly over Jaluit. However, wind shear (potential intensity) decreased (increased) near our site with a relatively unchanged mid-troposphere entropy gradient (Extended Data Fig. 6c–e), indicating that TCs generated in the positive GPI anomalies would continue intensification over Jaluit, despite the lower GPI driven by anomalously low ambient vorticity. Additionally, El Niño events occurring in this centennial mean state would likely increase the vorticity[39] and decrease the moist entropy gradient[24], further enhancing the GPI over Jaluit. However, the lack of inter-model agreement in the equatorial region for GPI and its individual components suggests that the anomalies there may not be a robust response to consistent forcing.

Spatially coherent shifts in environmental conditions generated most of the modelled GPI anomalies during the LIA. An anomalously large mid-troposphere moist entropy deficit across most of the western Pacific suppressed potential cyclogenesis in the models (Extended Data Fig. 6e). However, the modelled VWS anomalies were negative (positive) in the western (eastern) half of the basin, promoting (reducing) TC intensification, forming a zonal dipole in the tropics, which produced positive GPI anomalies in the SCS and east of the Philippines (Fig. 3b). Indeed, at either end of the tropical WNP, the LIA VWS anomaly exceeded the 95% confidence interval of anomalies from all 300-year periods in the Last Millennium experiment (Fig. 4a) and thus exceeded the model background variability. Background variability overwhelmed a similar zonal gradient formed by potential intensity anomalies (Fig. 4b).

Further analysis of the GCM ensemble revealed that the zonal dipole in anomalous VWS was generated by a westward shift in the rising arm of the PWC during the LIA (Fig. 4c,d). In the Last Millennium experiment, mean zonal winds converge at the surface and diverge at height within 130–180° E (Fig. 4c). At either end of the basin, mean zonal winds at the surface and top of the troposphere are opposed, generating high VWS. During the LIA and across the basin, zonal winds became more westerly at the surface and easterly at the top of the troposphere. These wind anomalies weakened (strengthened) shear in the west (east), where they opposed (bolstered) mean wind direction, producing the dipole in VWS anomalies (Fig. 4a). These wind anomalies would also shift the rising limb of the PWC westward, consistent with the hypothesized mechanism for a zonal concentration of precipitation in the IPWP[30].

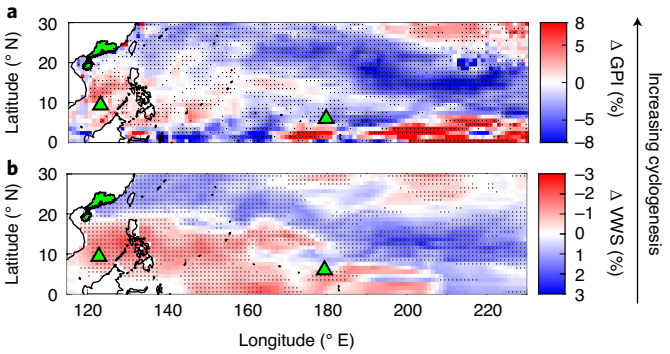

Fig. 3 | Change in tropical cyclogenesis potential from the MCA (1000–1300 CE) to the LIA (1400–1700 CE). a,**b**, Ensemble median relative anomaly (Δ = (LIA − MCA)/MCA × 100%) of (**a**) GPI and (**b**) VWS. Anomalies for all GPI components are plotted in Extended Data Fig. 5. Anomalies were calculated from Northern Hemisphere storm season (JASON) averages. The black stippling indicates that five of the seven models agree on change direction. The green symbols represent locations of storm reconstructions (Extended Data Fig. 1).

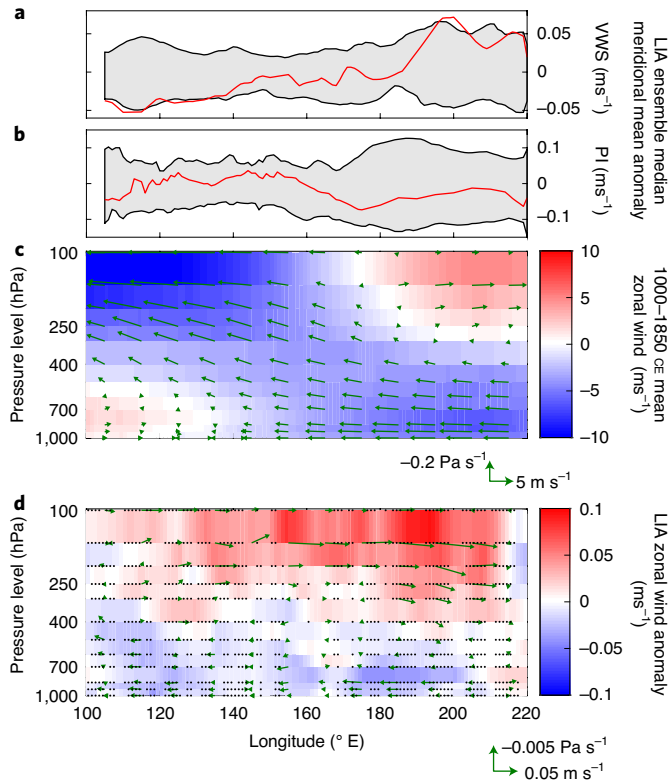

Fig. 4 | Relationship between vertical wind shear anomalies and the Pacific Walker circulation. a,**b**, Ensemble median of VWS (**a**) and PI (**b**) anomalies (red lines) during the LIA relative to 1000–1850 CE. **c**, Mean zonal wind (1000–1850 CE) (arrows, shading) and vertical pressure velocity (arrows). **d**, LIA anomaly of zonal wind (arrows, shading) and vertical pressure velocity (arrows). Grey shading in **a**,**b** encompasses the 95% confidence interval of ensemble medians from all 300-year periods within 1000–1850 CE. The stippling in **d** is as in Fig. 3. All quantities are ensemble medians and meridional averages over 0–20° N.

Influence of climate modes on tropical cyclone variability

The tropical zonal wind and VWS anomalies during the LIA are associated with centennial variability in the PMM. In the instrumental record, the PMM is a climate mode second only to ENSO in accounting for interannual variability of east tropical Pacific SST and wind anomalies[40]. Its positive (negative) phase is characterized by strengthened (weakened) meridional SST gradients across the mean latitude of the eastern Pacific ITCZ, northward (southward) shifts in the eastern Pacific ITCZ and weaker (stronger) trade winds in the eastern North Pacific. Positive (negative) PMM also generates anomalous VWS in the WNP, which causes an eastward (westward) shift in cyclogenesis[7,36]. Positive PMM events often precede and may initiate El Niño events[41], and the eastward shift in cyclogenesis previously associated with historical El Niño events may instead be a consequence of co-occurring positive PMM[36]. In our ensemble, the tropical VWS anomaly during the LIA is highly correlated (Fig. 5) with negative mean PMM during the LIA, in contrast to positive mean PMM during the MCA (Fig. 2f).

Proxy reconstructions of TC activity reveal that the transition from the end of the MCA through the early LIA was characterized by anomalously high TC activity in the deep tropical WNP. Although ENSO variability was lower over the last millennium relative to the instrumental period, transient increases in ENSO variability, when centennial mean climate conditions promoted cyclogenesis and intensification near reconstruction sites, could have generated this anomaly. The combination of periodic fluctuations in ENSO variability with secular changes to centennial mean climate conditions could explain spatial variability in TC activity across the west Pacific, whereas ascription to just one of these factors appears insufficient.

The GPI anomalies in our model ensemble are small relative to the anomalies in TC proxy reconstructions. Some of this discrepancy is likely explained by lower decadal to centennial variability in the Last Millennium experiment results relative to expectations based on paleoclimate proxy records[42–44]. For example, our model ensemble does produce anomalous meridional circulation during the LIA consistent with a contraction and southward shift of annual ITCZ movement (Extended Data Fig. 8). However, the magnitude of the modelled anomaly is only around 1% of the Last Millennium mean, which falls short of multi-degree latitude shifts interpreted from proxy records[29,32]. Even a one-degree southward shift in the ITCZ following a strong volcanic eruption in the tropical Northern Hemisphere can increase the GPI in the deep tropical North Pacific and decrease it poleward[45]. Thus, the model ensemble may have failed to capture additional LIA cyclogenesis variability associated with ITCZ shifts.

TC formation and intensification to typhoon strength in the Pacific near-equatorial region (0–5° N) are rare in the historical record, hindering analysis of trends and risk. Additionally, twenty-first century trends in TC genesis and track density for the Pacific deep tropics in the CMIP5 models are small, with low inter-model agreement on their direction[18,46]. CMIP5 GCMs may also not adequately resolve processes necessary for such perturbations to develop. Our reconstruction circumvents the limitations of historical records and GCMs and demonstrates that cyclogenesis in the Pacific deep tropics has centennial variability similar to that of TC landfalls captured in higher latitude reconstructions. Thus, TC climatology in the deep tropics is non-stationary, and lack of adequate historical sampling or inter-model agreement in projections does not necessarily indicate that TC genesis there has a muted response to climatic forcing.

The coincidence of major hydroclimate/regional atmospheric circulation shifts during the LIA with enhanced deep tropical cyclogenesis at Jaluit and in the SCS provides a basis for extrapolating TC climatological response to similar shifts projected for the twenty-first century. The PWC is projected to weaken and shift east[47,48], potentially reducing cyclogenesis in the SCS but promoting it in the Central Pacific. Additionally, recent tropical expansion due to anthropogenic warming and natural variability[49] has been

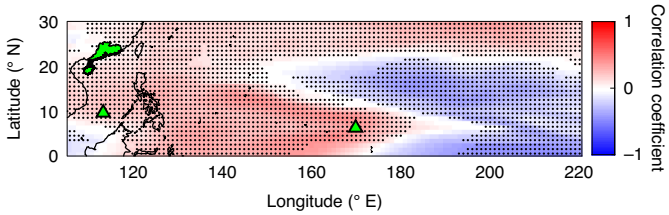

Fig. 5 | Ensemble median correlation between annual mean vertical wind shear and the PMM wind index in GCM ensemble results. The stippling indicates agreement on the direction of the correlation by at least five of the seven models. Model-specific correlation maps can be found in Extended Data Fig. 7.

connected with reduced cyclogenesis in the deep tropics and enhanced cyclogenesis at higher latitudes[35]. Our analysis suggests that anthropogenic radiative forcing may cause trends in Pacific deep tropical cyclogenesis that mirror the MCA–LIA transition, with cyclogenesis decreasing in the western deep tropical Pacific.

Online content

Any methods, additional references, Nature Research reporting summaries, source data, extended data, supplementary information, acknowledgements, peer review information; details of author contributions and competing interests; and statements of data and code availability are available at https://doi.org/10.1038/s41561-020-00656-2.

Received: 8 November 2019; Accepted: 6 October 2020;
Published online: 16 November 2020

References

1. Peduzzi, P. et al. Global trends in tropical cyclone risk. *Nat. Clim. Change* **2**, 289–294 (2012).
2. Emanuel, K., DesAutels, C., Holloway, C. & Korty, R. Environmental controls of tropical cyclone intensity. *J. Atmos. Sci.* **61**, 843–857 (2004).
3. Gray, W. M. Global view of the origin of tropical disturbances and storms. *Mon. Weather Rev.* **96**, 669–700 (1968).
4. Wu, L., Wen, Z., Huang, R. & Wu, R. Possible linkage between the monsoon trough variability and the tropical cyclone activity over the western North Pacific. *Mon. Weather Rev.* **140**, 140–150 (2012).
5. Brandon, C. M., Woodruff, J. D., Lane, P. & Donnelly, J. P. Tropical cyclone wind speed constraints from resultant storm surge deposition: a 2500 year reconstruction of hurricane activity from St. Marks, FL. *Geochem. Geophys. Geosyst.* **14**, 2993–3008 (2013).
6. van Hengstum, J. P. et al. The intertropical convergence zone modulates intense hurricane strikes on the western North Atlantic margin. *Sci. Rep.* **6**, 21728 (2016).
7. Gao, S., Zhi, L., Zhang, W. & Chen, Z. Strong modulation of the Pacific Meridional Mode on the occurrence of intense tropical cyclones over the western North Pacific. *J. Clim.* **31**, 7739–7749 (2018).
8. Huang, S. & Oey, L. Y. Land-falling typhoons are controlled by the meridional oscillation of the Kuroshio extension. *Clim. Dynam.* **52**, 2855–2867 (2018).
9. Woodruff, J. D., Kanamaru, K., Kundu, S. & Cook, T. L. Depositional evidence for the kamikaze typhoons and links to changes in typhoon climatology. *Geology* **43**, 91–94 (2015).
10. Liu, K., Shen, C. & Louie, K. A. 1,000-year history of typhoon landfalls in Guangdong, southern China, reconstructed from Chinese historical documentary records. *Ann. Assoc. Am. Geogr.* **91**, 453–464 (2001).
11. Yu, K. F., Zhao, J. X., Shi, Q. & Meng, Q. S. Reconstruction of storm/tsunami records over the last 4000 years using transported coral blocks and lagoon sediments in the southern South China Sea. *Quat. Int.* **195**, 128–137 (2009).
12. Donnelly, J. P. et al. Climate forcing of unprecedented intense-hurricane activity in the last 2000 years. *Earth's Future* **3**, 49–65 (2015).
13. van Hengstum, P. J. et al. Heightened hurricane activity on the Little Bahama Bank from 1350 to 1650 AD. *Cont. Shelf Res.* **86**, 103–115 (2014).
14. Lane, P., Donnelly, J. P., Woodruff, J. D. & Hawkes, A. D. A decadally-resolved paleohurricane record archived in the late Holocene sediments of a Florida sinkhole. *Mar. Geol.* **287**, 14–30 (2011).
15. Gischler, E., Shinn, E. A., Oschmann, W., Fiebig, J. & Buster, N. A. A 1500-year Holocene Caribbean climate archive from the Blue Hole, Lighthouse Reef, Belize. *J. Coast. Res.* **24**, 1495–1505 (2008).
16. Donnelly, J. P. et al. 700 yr sedimentary record of intense hurricane landfalls in southern New England. *Geol. Soc. Am. Bull.* **113**, 714–727 (2001).
17. Yan, Q., Wei, T. & Zhang, Z. Variations in large-scale tropical cyclone genesis factors over the western North Pacific in the PMIP3 last millennium simulations. *Clim. Dyn.* **48**, 957–970 (2016).
18. Zhang, L., Karnauskas, K. B., Donnelly, J. P. & Emanuel, K. Response of the North Pacific tropical cyclone climatology to global warming: application of dynamical downscaling to CMIP5 models. *J. Clim.* **30**, 1233–1243 (2017).
19. Blumenstock, D. I. Typhoon effects at Jaluit Atoll in the Marshall Islands. *Nature* **182**, 1267–1269 (1958).
20. Toomey, M. R., Donnelly, J. P. & Tierney, J. E. South Pacific hydrologic and cyclone variability during the last 3000 years. *Paleoceanography* **31**, 491–504 (2016).
21. Toomey, M. R., Donnelly, J. P. & Woodruff, J. D. Reconstructing mid-late Holocene cyclone variability in the Central Pacific using sedimentary records from Taha'a, French Polynesia. *Quat. Sci. Rev.* **77**, 181–189 (2013).
22. Kench, P. S., McLean, R. F., Owen, S. D., Tuck, M. & Ford, M. R. Storm-deposited coral blocks: a mechanism of island genesis, Tutaga Island, Funafuti Atoll, Tuvalu. *Geology* **46**, 915–918 (2018).
23. Kim, H. M., Webster, P. J. & Curry, J. A. Modulation of North Pacific tropical cyclone activity by three phases of ENSO. *J. Clim.* **24**, 1839–1849 (2011).
24. Patricola, C. M., Camargo, S. J., Klotzbach, P. J., Saravanan, R. & Chang, P. The influence of ENSO flavors on western North Pacific tropical cyclone activity. *J. Clim.* **31**, 5395–5416 (2018).
25. Denniston, R. F. et al. Extreme rainfall activity in the Australian tropics reflects changes in the El Niño/Southern Oscillation over the last two millennia. *Proc. Natl Acad. Sci. USA* **112**, 4576–4581 (2015).
26. Emile-Geay, J., Cobb, K. M., Mann, M. E. & Wittenberg, A. T. Estimating central equatorial Pacific SST variability over the past millennium. Part II: reconstructions and implications. *J. Clim.* **26**, 2329–2352 (2013).
27. Liu, Y. et al. Recent enhancement of central Pacific El Niño variability relative to last eight centuries. *Nat. Commun.* **8**, 15386 (2017).
28. Emile-Geay, J. et al. Links between tropical Pacific seasonal, interannual and orbital variability during the Holocene. *Nat. Geosci.* **9**, 168–173 (2015).
29. Denniston, R. F. et al. Expansion and contraction of the Indo-Pacific tropical rain belt over the last three millennia. *Sci. Rep.* **6**, 34485 (2016).
30. Yan, H. et al. South China Sea hydrological changes and Pacific Walker circulation variations over the last millennium. *Nat. Commun.* **2**, 293 (2011).
31. Yan, H. et al. Dynamics of the intertropical convergence zone over the western Pacific during the Little Ice Age. *Nat. Geosci.* **8**, 315–320 (2015).
32. Sachs, J. P. et al. Southward movement of the Pacific intertropical convergence zone AD 1400–1850. *Nat. Geosci.* **2**, 519–525 (2009).
33. Thompson, L. G. et al. Annually resolved ice core records of tropical climate variability over the past ~1800 years. *Science* **340**, 945–950 (2013).
34. Kossin, J. P., Emanuel, K. A. & Camargo, S. J. Past and projected changes in western North Pacific tropical cyclone exposure. *J. Clim.* **29**, 5725–5739 (2016).
35. Sharmila, S. & Walsh, K. J. E. Recent poleward shift of tropical cyclone formation linked to Hadley cell expansion. *Nat. Clim. Change* **8**, 730–736 (2018).
36. Hong, C. C., Lee, M. Y., Hsu, H. H. & Tseng, W. L. Distinct influences of the ENSO-like and PMM-like SST anomalies on the mean TC genesis location in the western North Pacific: the 2015 summer as an extreme example. *J. Clim.* **31**, 3049–3059 (2018).
37. Emanuel, K. & Nolan, D. Tropical cyclone activity and global climate. In *Proc. 26th Conference on Hurricanes and Tropical Meteorology* 240–241 (American Meteorological Society, 2004).
38. Emanuel, K. Tropical cyclone activity downscaled from NOAA-CIRES reanalysis, 1908–1958. *J. Adv. Model. Earth Syst.* **2**, 1 (2010).
39. Camargo, S. J., Emanuel, K. A. & Sobel, A. H. Use of a genesis potential index to diagnose ENSO effects on tropical cyclone genesis. *J. Clim.* **20**, 4819–4834 (2007).
40. Chiang, J. C. H. & Vimont, D. J. Analogous Pacific and Atlantic meridional modes of tropical atmosphere-ocean variability. *J. Clim.* **17**, 4143–4158 (2004).
41. Chang, P. et al. Pacific meridional mode and El Niño–Southern Oscillation. *Geophys. Res. Lett.* **34**, L16608 (2007).
42. PAGES Hydro2k Consortium. Comparing proxy and model estimates of hydroclimate variability and change over the Common Era. *Clim. Past* **13**, 1851–1900 (2017).
43. Ault, T. R., Deser, C., Newman, M. & Emile-Geay, J. Characterizing decadal to centennial variability in the equatorial Pacific during the last millennium. *Geophys. Res. Lett.* **40**, 3450–3456 (2013).
44. Zanchettin, D., Rubino, A., Matei, D., Bothe, O. & Jungclaus, J. H. Multidecadal-to-centennial SST variability in the MPI-ESM simulation ensemble for the last millennium. *Clim. Dyn.* **40**, 1301–1318 (2013).

45. Pausata, F. S. R. & Camargo, S. J. Tropical cyclone activity affected by volcanically-induced ITCZ shifts. *Proc. Natl Acad. Sci. USA* **116**, 7732–7737 (2019).
46. Camargo, S. J. Global and regional aspects of tropical cyclone activity in the CMIP5 models. *J. Clim.* **26**, 9880–9902 (2013).
47. Chung, E. S. et al. Reconciling opposing Walker circulation trends in observations and model projections. *Nat. Clim. Change* **9**, 405–412 (2019).
48. Vecchi, G. A. & Soden, B. J. Increased tropical Atlantic wind shear in model projections of global warming. *Geophys. Res. Lett.* **34**, L08702 (2007).
49. Staten, P. W. et al. Tropical widening: from global variations to regional impacts. *Bull. Amer. Meteor. Soc.* **101**, E897–E904 (2020).
50. Cobb, K. M. et al. Highly variable El Niño–Southern Oscillation throughout the Holocene. *Science* **339**, 67–70 (2013).

Methods

Study site and field methods. We developed a sediment proxy reconstruction of TC activity at Jaluit Atoll in the southern Marshall Islands. Jaluit is a mid-ocean atoll with a 250–1,000-m-wide intertidal reef flat encircling a shallow lagoon. The mildly stratified blue hole from which we extracted sediment cores LTD2 and LTD3 is located at the northwestern tip of Jaluit, where the atoll rim is the widest (Extended Data Fig. 1). The blue hole is flanked by three small, vegetated islands between which smooth channels connect it to the ocean-facing reef flat, which is covered in crustose coralline algae. The blue hole is backed by a deeper 400-m-wide reef flat with actively growing coral.

The sediment cores were retrieved using a Rossfelder P-3 vibracoring system. For core LTD2, a separate surface drive of the upper 1–1.5 m of sediment was retrieved to preserve the sediment surface, because the primary drive over-penetrated. Coring sites were selected based on bathymetry and absence of hard substrate such as large coral heads. Bathymetry and seismic surveys were recorded using an EdgeTech 3100 Chirp sub-bottom sonar system with a 4–24 kHz fish towed behind a small outboard-motor craft. The cores were sectioned in the field before transportation to the lab.

Laboratory analysis. The cores were split and described in the lab (SI Core descriptions) and then sampled at 1-cm intervals. Samples were wet-sieved at 63 μm and dry-sieved at 250 and 2,000 μm to obtain dry weight-normalized grain-size fractions at each sieve size.

We established age controls for each core with a series of accelerator mass spectrometer (AMS) radiocarbon dates (Extended Data Table 1) and assumed core-top dates. Where available, we sampled terrestrial organic macrofossils for dating, but they were rare, especially below the first few meters. Most of our core dates were measured from detrital inorganic carbonate and thus have reduced precision and greater uncertainty due to the marine reservoir effect. All radiocarbon dating was performed at the National Ocean Sciences Accelerator Mass Spectrometer (NOSAMS, Woods Hole, Massachusetts, United States) facility. Sediment at the top of each core was assumed deposited immediately prior to core extraction in November 2015. The top core section of the LTD2 primary drive did not capture the sediment–water interface; hence, the location of the core top was inferred from the separate surface drive using a near-surface tie point. Using tie points in this manner assumes that the deposition rate in the vicinity of the core top is equal between the primary and surface drive. For LTD2, we used the base of a large coarse event bed as a tie point (Extended Data Fig. 2). The base of a large storm event bed common to all LTD2 and LTD3 drives was used as an additional tie point for LTD3 age control (Supplementary Methods).

The LTD3 age model (Extended Data Fig. 2) was generated using the Bayesian age modelling software BACON[51], with the IntCal13 curve for terrestrial organic carbon dates[52], the Marine13 curve for inorganic carbon dates from detrital carbonate sediment grains[52] and the Northern Hemisphere Zone 3 (ITCZ region) post-bomb curve for one post-bomb date[53]. BACON constructs an ensemble of accumulation histories through Markov chain Monte Carlo iteration on the provided dates and thus provides a distribution of likely ages for every centimetre of the core. Inorganic carbonate dates were corrected for a marine reservoir effect using $\Delta R = 41 \pm 42$ yr, determined for the past 2,500 years from branching coral samples retrieved from Ebon Atoll, Republic of the Marshall Islands, 200 km southwest of the Jaluit blue hole[54].

Event bed selection. We performed a simple statistical analysis of sediment grain size to identify event beds in our cores (Extended Data Fig. 3). First, outliers were identified as samples of the coarse fraction that exceeded the mean coarse fraction by 2 standard deviations; both statistics were calculated within an 11-cm moving window, encompassing roughly 50 years according to the age model. Then, the moving average was recalculated, but this time, the outliers were excluded. Finally, event beds were identified as peaks in the moving-average-subtracted coarse fraction anomaly that exceeded the coarse fraction by 1.5 standard deviations, calculated for the entire core excluding the outliers. Removing outliers from the analysis prevented particularly large event beds from masking the presence of smaller peaks nearby, and using the moving window removed the influence of decadal variability in the background coarse fraction signal. We found that increasing the window size, increasing the threshold coarse anomaly and including outliers affected the absolute number of event beds identified but did not change the qualitative patterns in event bed frequency in core LTD3 (Extended Data Figs. 4 and 5). For the statistical analysis, we used the coarse fraction with sieve diameter between 250 μm and 2 mm to account for the anomalous transport characteristics of very coarse bioclastic sediment (Supplementary Methods).

We calculated centennial event frequency using a procedure that incorporates uncertainty in the age model. For every identified storm event bed, we randomly sampled 9,000 ages from the Bayesian age model ensemble, and from them, we constructed a probability distribution function (PDF) with annual resolution. We then summed the values of all PDFs within a 100-year moving window, resulting in a time series of continuous centennial event frequency estimates incorporating relative uncertainty and age model shape for each event (Extended Data Fig. 3). We modelled centennial event frequency in the record as a Poisson process and estimated a record-wide mean (95% confidence interval) event frequency of $\lambda = 0.95$ (0.64–1.36) events per century at Jaluit by counting all identified event beds and dividing by the length of time captured by the core. As an alternative measure of mean event frequency, we examined 25,500 TCs dynamically downscaled for NCEP reanalysis climatology for the years 1996–2010 (see ref. [18] for details). TCs with sustained wind speeds > 64 m s^{-1} (super typhoon/Category 4–5) passed within 75 km of the blue hole with a modern frequency of $\lambda = 1.39$ events per century.

Inactive intervals in the core were identified as periods of time with zero events whose duration exceeded the 95% confidence interval (3–388 years) of a gamma distribution governing the time intervals between single events, with occurrence rate defined by the proxy Poisson process above. Active intervals are more difficult to define statistically, as different numbers of events occurring over different interval lengths can have the same probability of random occurrence. Thus, active intervals were first identified as those intervals in the frequency time series where the event frequency exceeded the 95% confidence interval of the Poisson distribution mean frequency for at least one century (Extended Data Figs. 4 and 5). The probability that each active interval was generated randomly (unforced) was then estimated using the cumulative distribution function of a gamma distribution defined by the proxy Poisson process above and the number of events contributing to the active interval, evaluated for the time interval between the first and last events. For example, 10 events make up the active interval roughly concurrent with the LIA, and the first and last occur at 1345 and 1634 CE, respectively. The probability that this interval was the random result of a Poisson process is $p < 0.001$ for $\lambda = 0.95$ events per century and $p = 0.008$ for the higher $\lambda = 1.39$ events per century. Under the simplifying assumption that our 3,609-year record represents $3{,}609/289 = 12.5$ independent draws from this gamma distribution, the chances that the LIA peak would be randomly generated in any similar-length record would be 1.2% for $\lambda = 0.95$ events per century and 9.6% for $\lambda = 1.39$ events per century.

Best track analysis. To illustrate modern TC genesis and tracks in the vicinity of our reconstruction site under modern climate conditions, we calculated simple statistics on six-hourly best track data from IBTrACS-WMO, v03r10[55], for western Pacific and eastern Pacific basins for the period January 1848 to June 2017.

Climate model analysis. We used the results from seven GCMs to explore possible drivers of anomalous TC climatology during the LIA. We used every model involved in the fifth iteration of CMIP that provided results for the Last Millennium experiment (Extended Data Table 2), except for the Model for Interdisciplinary Research on Climate Earth System Model (MIROC-ESM), which was excluded because of its long-term drift[56]. Removal of FGOALS-g1 from the ensemble, leaving only one FGOALS member, did not qualitatively alter the results but reduced inter-model agreement. We used monthly mean values for all our analyses.

We quantified TC genesis potential using the genesis potential index (GPI)[37,38]:

$$\mathrm{GPI} = |\eta|^3 \chi^{-4/3} \mathrm{MAX}(\mathrm{PI} - 35\ \mathrm{ms}^{-1}, 0)^2 (25\ \mathrm{ms}^{-1} + \mathrm{VWS})^{-4}$$

where η is the absolute vorticity at 850 hPa, χ is a measure of the moist entropy deficit of the middle troposphere and represents an entropy gradient barrier to cyclone intensification[57], PI is potential intensity, an estimate of maximum achievable wind speeds as a function of convectively available potential energy[58] and VWS is absolute wind shear between 250 hPa and 850 hPa. As can be inferred from the sign of the exponent applied to each variable, vorticity and potential intensity tend to promote TC formation and intensification, respectively, while the moist entropy deficit and wind shear tend to depress or interrupt formation and intensification, respectively.

Here, we define vertical wind shear (VWS) as the difference between winds at 850 hPa and 250 hPa to be consistent with previous research defining and applying the GPI[18,38,59]. However, some previous work has instead used the difference in winds at 850 hPa and 200 hPa to define VWS and alternative TC genesis indexes. We investigated vertical profiles of mean winds in the western North Pacific and found that the variability (with and without seasonality included) of 200 hPa and 250 hPa winds is highly correlated in the Last Millennium experiment model results. Additionally, recalculating GPI and VWS using 200 hPa winds did not qualitatively affect our results. Additionally, ignoring the components of the GPI that have historically not correlated strongly with temporal trends in cyclogenesis did not affect our results qualitatively (see Supplementary Discussion).

The GPI was calculated using the monthly mean climate model output. In reality, TCs would be expected to respond to variability in the input variables over daily or sub-daily timescales, and such variability is lost when calculating, for example, vertical shear from monthly mean wind velocity instead of taking the monthly mean of daily VWS. Previous research has found that trends in VWS change little regardless of whether they are calculated from daily mean or monthly mean wind velocity and then averaged over longer climatological timescales[48,60]. Here, we assume that calculating the GPI using higher temporal resolution model output would not alter our results qualitatively.

We calculated the GPI and all its components at the native spatial resolution of each model before interpolating linearly to a common 1° × 1° grid. Relative anomalies in each index between the LIA (1400–1700 CE) and the MCA (1000–1300 CE) were calculated according to (LIA − MCA)/MCA × 100% for each model. Multi-model ensemble averaging was performed using the median statistic

as the last step in any analysis where it is presented (for example, percent change between the MCA and the LIA was calculated for each model separately and the median was then taken for a multi-model ensemble value and displayed in Fig. 3). For all comparisons, time averages include only values from the primary storm season, that is, July–November (JASON) in the North Pacific.

To determine the magnitude of VWS (potential intensity) anomalies during the LIA relative to variability throughout the last millennium, we conducted a bootstrap analysis in which we calculated the ensemble median, meridional mean shear (potential intensity) anomaly, relative to the Last Millennium mean, for every 300-year period within the Last Millennium experiment results. From these populations, we calculated the 95% confidence intervals of the anomalies at each longitude.

The PMM indexes were calculated from the SST and meridional and zonal surface wind fields for 20° S–30° N, 150–265° E. First, the influence of ENSO variability on the fields was removed by subtracting a linear least-squares fit between the fields and the cold tongue index, as in Chiang and Vimont[40]. Maximum covariance analysis was then applied to the cross-covariance matrix between the SST and both wind fields (with land cells masked out). The PMM SST and wind indexes were identified with the second mode for the 1000–1850 CE period. We measured the correspondence between the mean annual storm season PMM and the VWS using Spearman's rank correlation for the years 1000–1850 CE. The statistical significance was calculated using a two-tailed Student's t-test after taking multiple testing into account with application of the false discovery rate procedure and setting $q = 2.5\%$[61].

Data availability

Grain-size data, median ages by depth, centennial event frequency and the dated material for core LTD3 are available from the National Oceanic and Atmospheric Administration National Centers for Environmental Information (NCEI) paleoclimatology database https://www.ncdc.noaa.gov/paleo/study/31132 and can also be found on the Woods Hole Open Access Server (WHOAS), https://doi.org/10.26025/1912/26159. Much of the data from the existing literature plotted in Fig. 2 can be found on the NCEI paleoclimatology database (https://www.ncdc.noaa.gov/paleo-search/) using the following data set ids: Fig. 2a [noaa-recon-13684], Fig. 2b [noaa-coral-13672], Fig. 2c [noaa-lake-29432], Fig. 2d [noaa-icecore-14174], Fig. 2e [noaa-cave-20530]. Data for Fig. 1b,c are available as tables at https://doi.org/10.1016/j.quascirev.2013.07.019[21] and in the supplementary information at https://doi.org/10.1002/2015PA002870[20].

Code availability

The MATLAB code used to analyse the GCM output and the code and data used to plot the figures are available on the Woods Hole Open Access Server (WHOAS), https://doi.org/10.26025/1912/26159.

References

51. Blauuw, M. & Christen, J. A. Flexible paleoclimate age-depth models using an autoregressive gamma process. *Bayesian Anal.* **6**, 457–474 (2011).
52. Reimer et al. IntCal13 and Marine13 radiocarbon age calibration curves 0–50,000 years cal BP. *Radiocarbon* **55**, 1869–1887 (2013).
53. Hua, Q., Barbetti, M. & Rakowski, A. Z. Atmospheric radiocarbon for the period 1950–2010. *Radiocarbon* **55**, 2059–2072 (2013).
54. Weisler et al. Marine reservoir correction for the southern Marshall Islands for the past 2500 years. *Radiocarbon* **60**, 333–348 (2018).
55. Knapp, K. R., Kruk, M. C., Levinson, D. H., Diamond, H. J. & Neumann, C. J. The international best track archive for climate stewardship (IBTrACS) unifying tropical cyclone data. *Bull. Am. Meteorol. Soc.* **91**, 363–376 (2010).
56. Sueyoshi et al. Set-up of the PMIP3 paleoclimate experiments conducted using an earth system model, MIROC-ESM. *Geosci. Model Dev.* **6**, 819–836 (2013).
57. Emanuel, K. A., Sundararajan, R. & Williams, J. Hurricanes and global warming: results from downscaling IPCC AR4 simulations. *Bull. Am. Meteorol. Soc.* **89**, 347–367 (2008).
58. Bister, M. & Emanuel, K. A. Dissipative heating and hurricane intensity. *Meteorol. Atmos. Phys.* **65**, 233–240 (1998).
59. Emanuel, K. A. Downscaling CMIP5 climate models shows increased tropical cyclone activity over the 21st century. *Proc. Natl Acad. Sci. USA* **110**, 12219–12224 (2013).
60. Korty, R. L., Camargo, S. J. & Galewsky, J. Tropical cyclone genesis factors in simulations of the Last Glacial Maximum. *J. Clim.* **25**, 4348–4365 (2012).
61. Hu, J., Emile-Geay, J. & Partin, J. Correlation-based interpretations of paleoclimate data – where statistics meet past climates. *Earth Planet. Sci. Lett.* **459**, 362–371 (2017).

Acknowledgements

We thank student intern D. Carter for extensive labwork on core LTD3. This work was supported by the Strategic Environmental Research and Development Program (SERDP RC-2336). C.C.U. acknowledges support from NSF under AGS-1602455. We acknowledge the WCRP's Working Group on Coupled Modelling, which is responsible for CMIP, and we thank the climate modelling groups for producing and making available their model output. CMIP5 model output was provided by the WHOI CMIP5 Community Storage Server via their website: http://cmip5.whoi.edu/. Any use of trade, firm or product names is for descriptive purposes only and does not imply endorsement by the US Government.

Author contributions

J.F.B. performed the labwork and model analysis, and wrote the initial draft. J.F.B., M.R.F., P.S.K., A.D.A., M.R.T., R.M.S. and J.P.D. performed the fieldwork and advised on sedimentology analysis and interpretation. K.B.K. and C.C.U. advised on model analysis and interpretation. All authors discussed the results, commented on the manuscript and contributed revisions.

Competing interests

The authors declare no competing interests.

Additional information

Extended data is available for this paper at https://doi.org/10.1038/s41561-020-00656-2.

Supplementary information is available for this paper at https://doi.org/10.1038/s41561-020-00656-2.

Correspondence and requests for materials should be addressed to J.F.B.

Peer review information Primary Handling Editor(s): James Super.

Reprints and permissions information is available at www.nature.com/reprints.

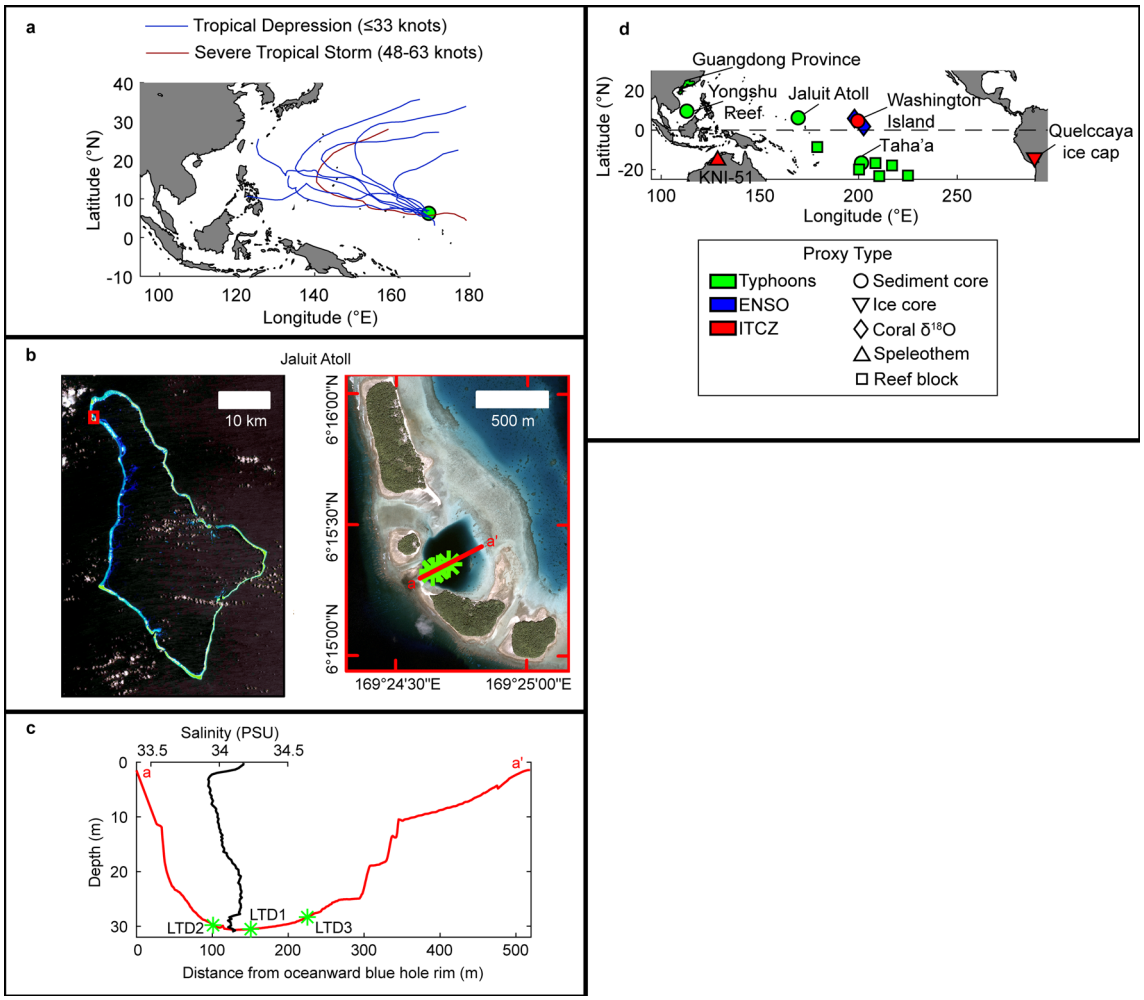

Extended Data Fig. 1 | Maps of the reconstruction site. Maps of the reconstruction site: **a**, Map of the tropical western Pacific, with the storm tracks of every tropical cyclone in the IBTrACS dataset to pass within 100 km of Jaluit Atoll; **b**, map of the site showing location of cores as green asterisks; **c**, bathymetric profile of the basin from which the sediment cores were extracted, with a salinity profile; **d**, map of the tropical Pacific with locations of the reconstructions referenced in this study.

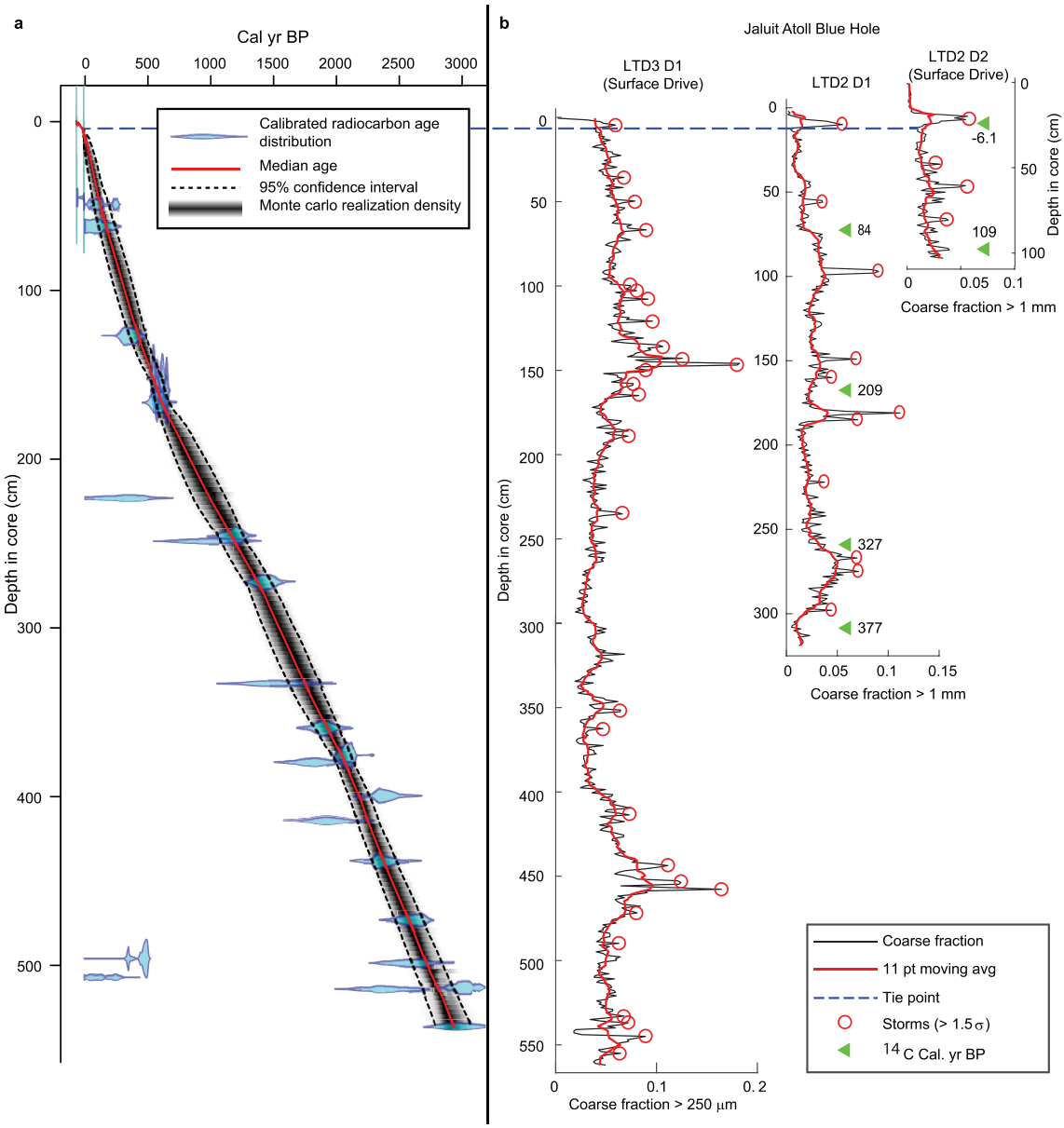

Extended Data Fig. 2 | Profiles of sediment cores collected from the Jaluit Atoll blue hole. Profiles of sediment cores collected from the Jaluit Atoll blue hole. **a**, BACON age model for LTD3 and **b**, coarse fraction profiles of LTD2 and LTD3. BACON-calibrated radiocarbon dates are displayed as green triangles. A tie point used in the age models and to establish core top depth by comparing drives are indicated with a blue dashed line. Storm beds were identified as those samples that exceeded 1.5 standard deviations above an 11-cm moving average, where both statistics were calculated while ignoring >2 standard deviation outliers.

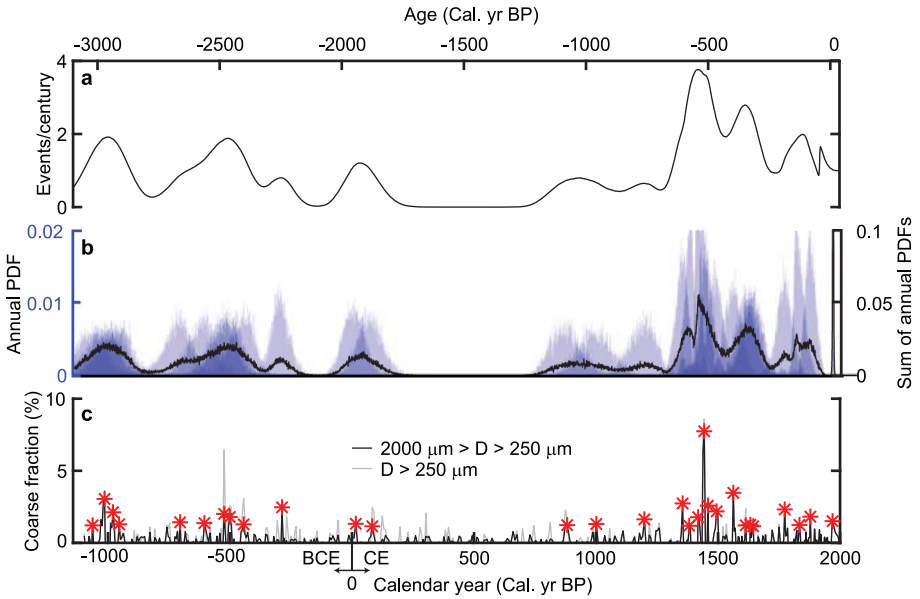

Extended Data Fig. 3 | Illustration of the method used to calculate centennial event frequency from coarse fraction. Illustration of the method used to calculate centennial event frequency from coarse fraction. **c**, Coarse fraction anomaly is used to identify event deposits as in Methods. **b**, The annually-binned probability distribution function (PDF, blue shading) of each event deposit is extracted from the age model and summed for each year (black line). **a**, The sum of annual PDFs is summed over a 100-year moving window to construct a time series of centennial event frequency incorporating age model uncertainty.

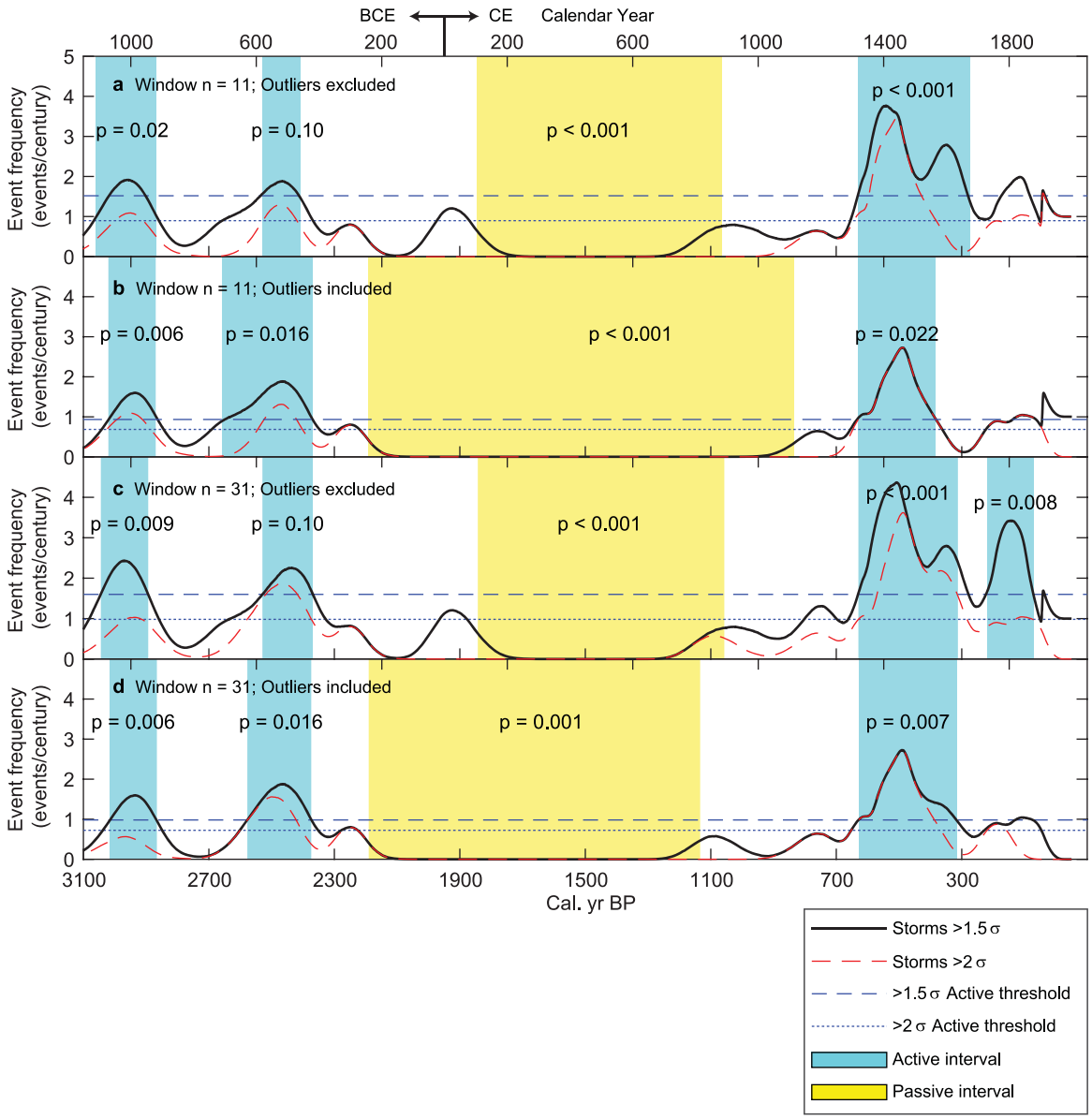

Extended Data Fig. 4 | Sensitivity analysis of the procedure used to identify event beds in Jaluit Atoll core LTD3 grain size data, using the 250–2000 µm coarse fraction. Sensitivity analysis of the procedure used to identify event beds in Jaluit Atoll core, LTD3 grain size data, using the 250–2000 µm coarse fraction. Coarse fraction variance over the entire core was calculated **a**, with a moving-average window-size of 11 cm and exclusion of outliers, **b**, with a moving average window size of 11 cm and inclusion of outliers, **c**, with a moving average window size of 31 cm and exclusion of outliers, and **d**, with a moving average window size of 31 cm and inclusion of outliers. For each of these four cases, event beds were flagged with 1.5 standard deviation and 2 standard deviation cutoffs. The active interval thresholds for each of these cutoffs represents the 97.5 percentile frequency for a Poisson distribution with the core's mean event frequency. Active intervals were identified as intervals lasting at least a century in which those thresholds were exceeded. Passive intervals were identified as intervals with zero events that were less than 2.5% likely to occur according to a gamma distribution. P-values are the cumulative frequency distribution values for a gamma distribution defined by a Poisson process defined by the cores centennial event frequency and the number of events contained in an active or passive interval, evaluated for the length of time between the first and last event in that interval.

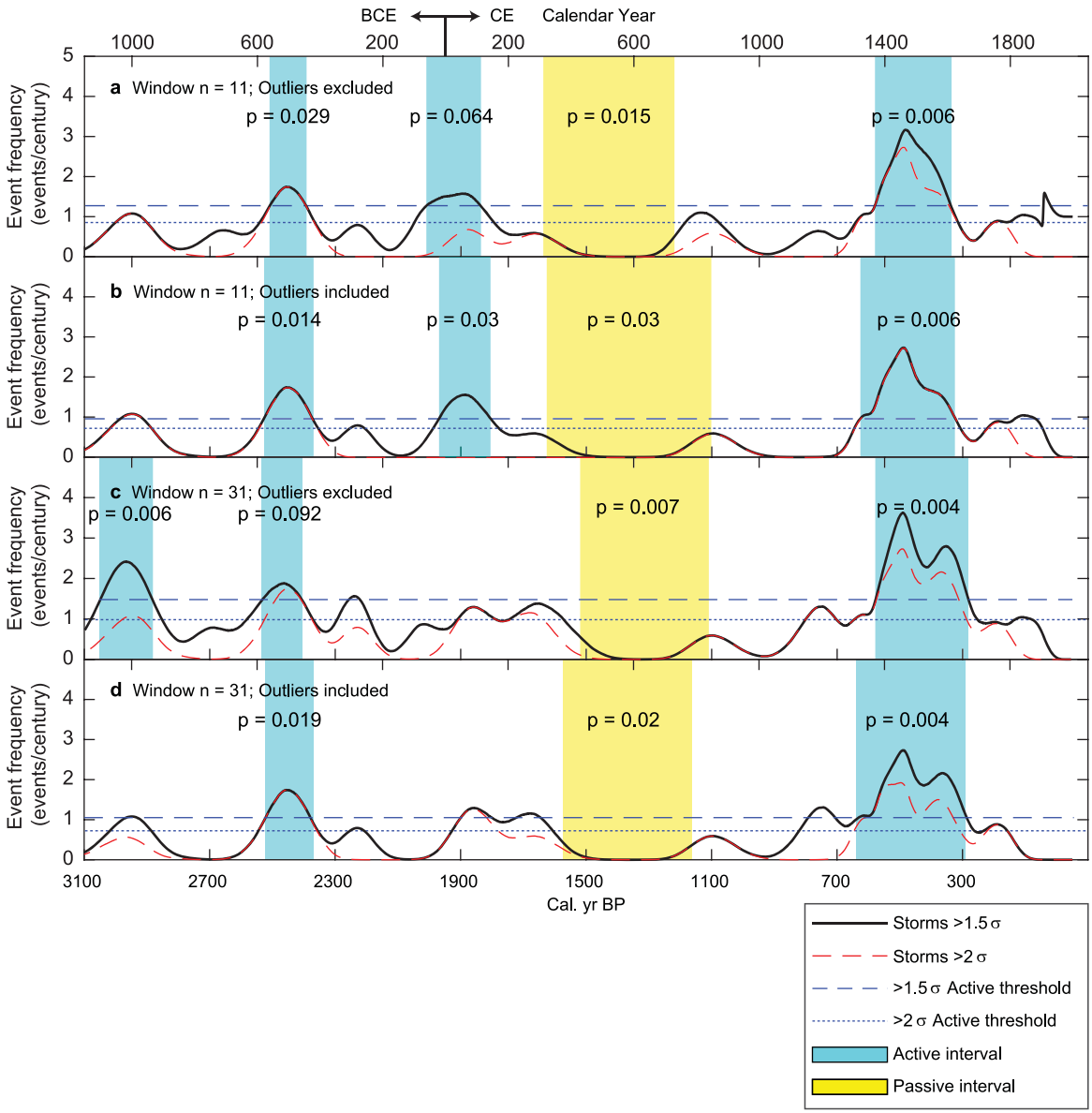

Extended Data Fig. 5 | Same as ED Fig. 4, but using the >250 µm coarse fraction. Same as Extended Data Fig. 4, but using the >250 µm coarse fraction.

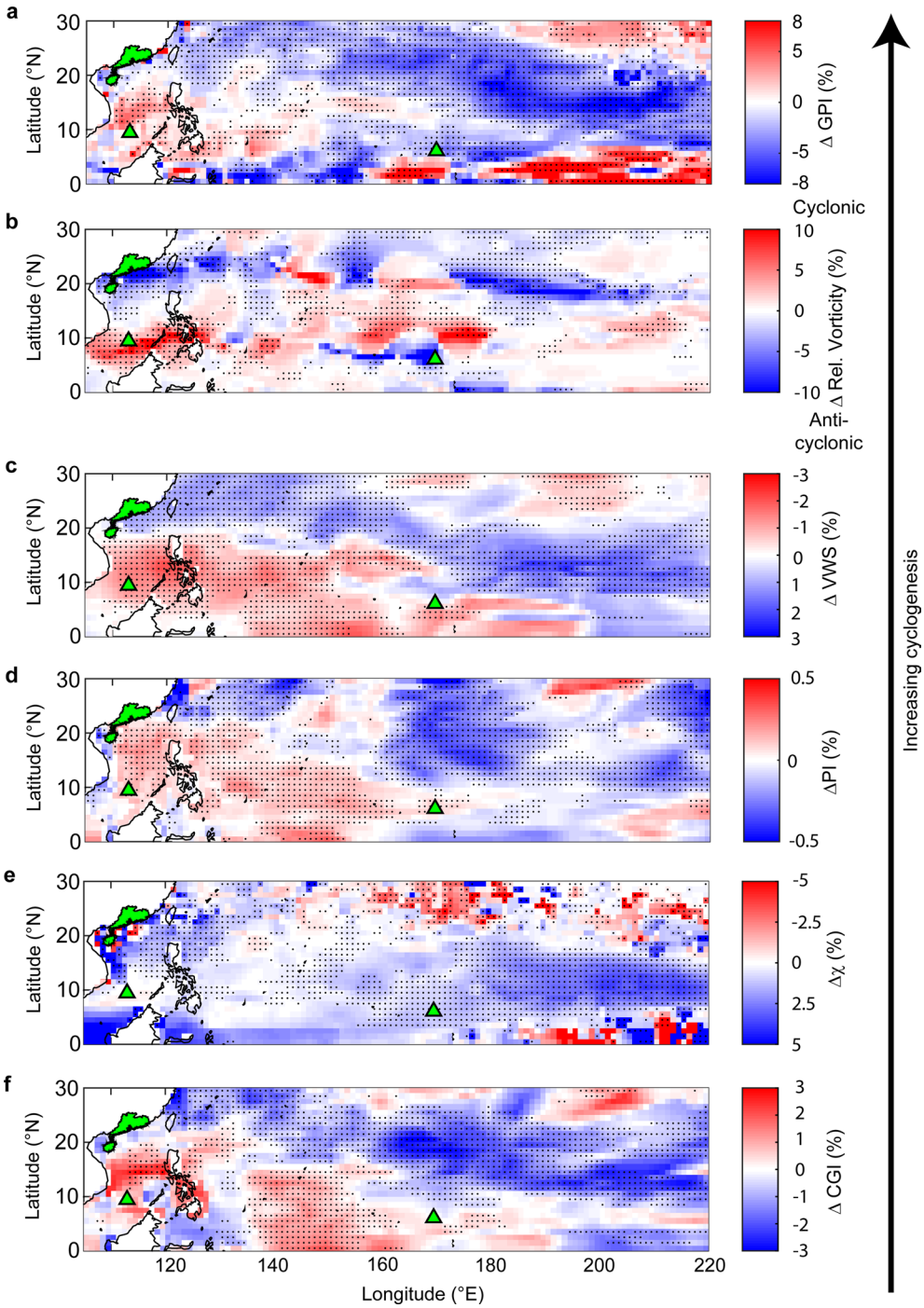

Extended Data Fig. 6 | Ensemble median relative anomaly in tropical cyclone genesis indexes during the Little Ice Age (1400–1700 CE). Ensemble median relative anomaly in tropical cyclone genesis indexes during the LIA (1400–1700 CE). Relative anomaly was calculated as Δ = (LIA - MCA) / MCA $\times$ 100%. The **a**, Genesis Potential Index[41] is calculated from four variables: **b**, low level vorticity, η (s^{-1}), **c**, vertical wind shear (ms^{-1}), **d**, potential intensity (ms^{-1}), and **e**, the mid-troposphere saturation deficit, χ (dimensionless)[57]. The colour palettes are aligned so red always indicates increasing cyclogenesis potential. The sign of relative vorticity in the southern hemisphere in b) was reversed so positive change indicates more cyclonic vorticity. Percent change values were calculated from storm season averages for the two time periods. In the northern hemisphere, the WNP storm season (JASON) was used. No data is shown for 1°S-1°N to indicate the different months used for averaging in each hemisphere. Black stippling indicates grid cells in which at least five of seven models agreed on the direction of change. The green symbols represent the locations of storm reconstructions (Extended Data Fig. 1).

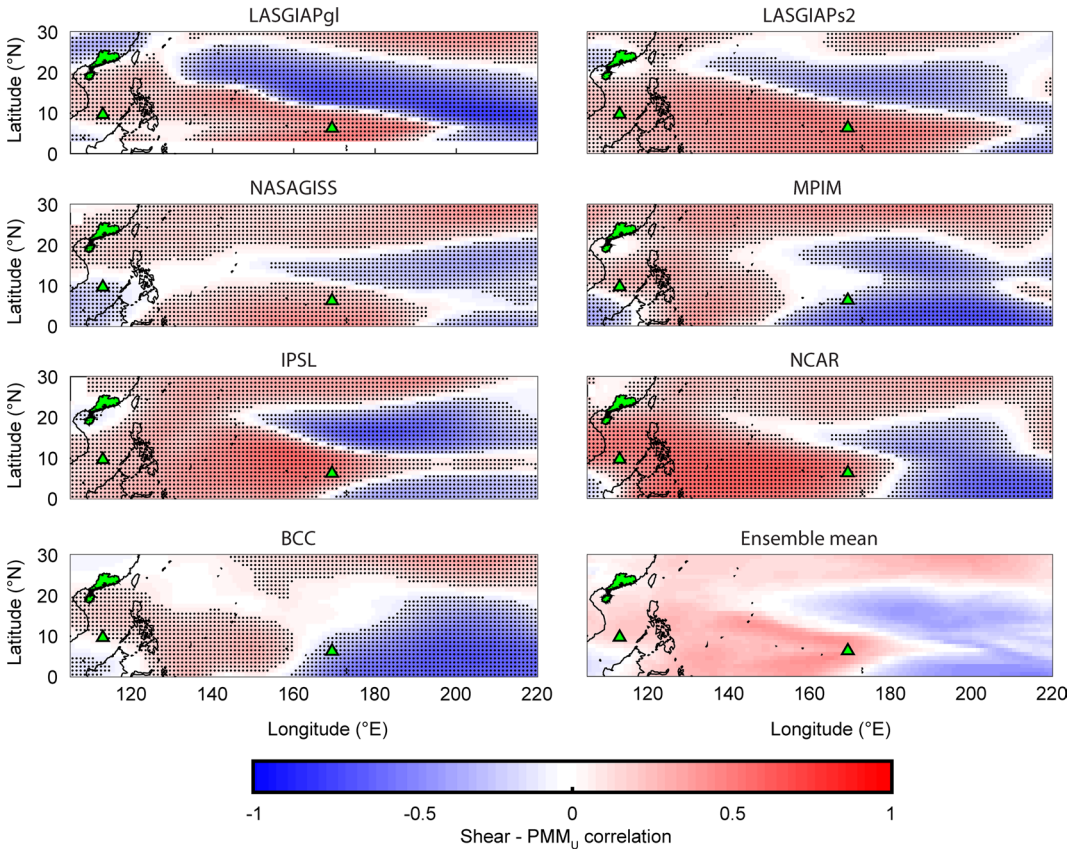

Extended Data Fig. 7 | Spearman rank correlation between mean storm season vertical wind shear and Pacific Meridional Mode for each of the CMIP5 models. Spearman rank correlation between mean storm season vertical wind shear and Pacific Meridional Mode for each of the CMIP5 models. Correlation coefficients were calculated for Last Millennium experiment results for the period 1000–1850 CE. Black stippling indicates statistical significance as determined by a two-tailed Student t-test after taking into account multiple hypothesis testing using the false discovery rate procedure and setting q = 2.5%[61].

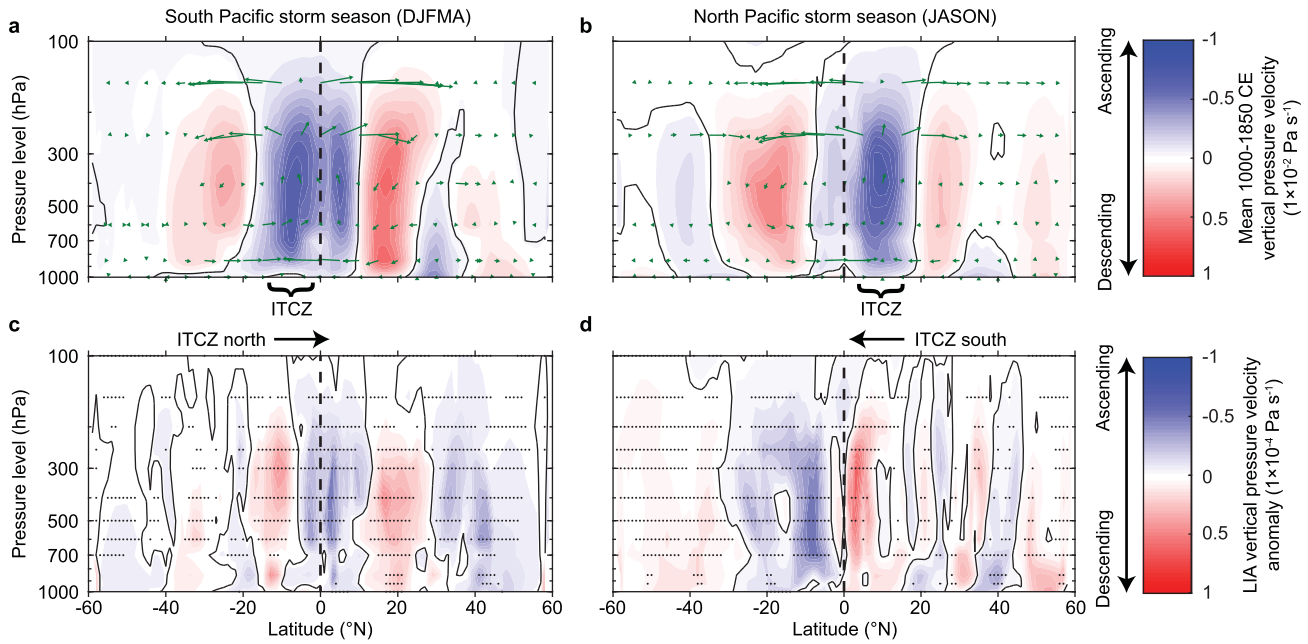

Extended Data Fig. 8 | Hadley circulation anomalies during the Little Ice Age (1400–1700 CE). Hadley circulation anomalies during the Little Ice Age (1400–1700 CE). Zonal (100–180°E) mean vertical pressure velocity associated with meridional overturning circulation (shading, vectors) and non-divergent meridional wind velocity (vectors) **a**,**b**, averaged over 1000–1850 CE and **c**,**d**, the LIA (1400–1700 CE) anomaly relative to 1000–1850 CE. The dashed vertical lines indicate the equator. Negative (positive) vertical pressure velocity values indicate ascending (descending) motion. Black stippling in c,d) indicates pressure/latitude coordinates where at least 5 of the 7 models agreed on the direction of change.

Core/ Drive	Sample Name	Accession #	Sample contents	Drive depth (cm)	^{14}C age (yr)	^{14}C error (yr)
LTD2/D2	LTD2_D2_1:1_22-23cm	OS-133794	Plant/wood	23	-5.645	0.25
LTD2/D2	LTD2_D2_1:1_105.5cm	OS-129304	Plant/wood	106	125	15
LTD2/D1	LTD2_D1_1:3_72cm†	OS-128853	Coral	72	550	20
LTD2/D1	LTD2_D1_2:3_64cm†	OS-128854	Coral	167	545	15
LTD2/D1	LTD2_D1_3:3_35-36cm	OS-127189	Plant/wood	259	350	15
LTD2/D1	LTD2_D1_3:3_84.5	OS-127190	Plant/wood	308	330	15
LTD3/D1	LTD3_D1_1:5_45*	OS-127347	Plant/wood	45	-465	16
LTD3/D1	LTD3_D1_1:5_48-49cm	OS-133795	Plant/wood	49	110	20
LTD3/D1	LTD3_D1_1:5_62cm†	OS-128851	Mollusc	62	515	15
LTD3/D1	LTD3_D1_2of5_25-26cm†	OS-151049	Foraminifera	126.5	735	15
LTD3/D1	LTD3_D1_2:5_52	OS-127191	Plant/wood	152.5	560	15
LTD3/D1	LTD3_D1_2:5_59.5cm†	OS-129133	Halimeda	160	660	15
LTD3/D1	LTD3_D1_2of5_65-66cm†	OS-151050	Foraminifera	166.5	1040	15
LTD3/D1	LTD3-D1-3of5-3.5cm††*	OS-139903	Mollusc	223	740	160
LTD3/D1	LTD3_D1_3of5_25-26cm†	OS-151051	Mollusc	245	1,670	25
LTD3/D1	LTD3-D1-3of5-29cn††	OS-139904	Mollusc	248.5	1,460	160
LTD3/D1	LTD3_D1_3of5_52-53cm†	OS-151052	Foraminifera	272	1,930	25
LTD3/D1	LTD3-D1-3of5-113.5cm††	OS-139901	Mollusc	333	1,980	160
LTD3/D1	LTD3_D1_4of5_20-21cm†	OS-151053	Foraminifera	359.5	2,330	25
LTD3/D1	LTD3_D1_4of5_36-37cm	OS-149473	Plant/wood	375.5	2,110	20
LTD3/D1	LTD3_D1_4_41††	OS-125137	Mollusc	379.5	2,260	80
LTD3/D1	LTD3_D1_4of5_60-61cm†	OS-151054	Foraminifera	399.5	2,720	25
LTD3/D1	LTD3_D1_4_75p5††	OS-125138	Mollusc	414	2,350	80
LTD3/D1	LTD3_D1_4of5_99-100cm†	OS-151055	Foraminifera	438.5	2,700	30
LTD3/D1	LTD3_D1_5of5_12-13cm†	OS-151056	Foraminifera	481.5	2,890	20
LTD3/D1	LTD3_D1_5of5_36cm*	OS-141714	Plant/wood	496	390	20
LTD3/D1	LTD3_D1_5_38††	OS-125134	Mollusc	498.5	2,890	90
LTD3/D1	LTD3_D1_5of5_46.5cm*	OS-149409	Plant/wood	507	60	100
LTD3/D1	LTD3_D1_5of5_52-53cm†	OS-151057	Foraminifera	513	2,930	20
LTD3/D1	LTD3_D1_5_53p5††	OS-125136	Mollusc	514	2,710	90
LTD3/D1	LTD3_D1_5_75p5††	OS-125135	Mollusc	536	3,210	85

† Indicates inorganic carbonate sample processed with hydrolysis and conventional AMS.

†† Indicates inorganic carbonate sample processed with gas ion source. All samples were processed at NOSAMS.

* Indicates outliers excluded from the age model (SI Core descriptions).

Extended Data Fig. 9 | Sediment core radiocarbon dates.

Institute	Model	Country	LM Years CE	Atmospheric resolution Latitude (°)	Longitude (°)
BCC	BCC-CSM1.1	China	850-2000	2.81	2.81
NASA	GISS-E2-R	USA	850-1850	2.00	2.50
IPSL	IPSL-CM5A-LR	France	850-1850	1.89	3.75
LASG-IAP	FGOALS-g1	China	1000-2000	4.00	5.00
LASG-IAP	FGOALS-s2	China	850-1850	1.71	2.81
MPI-M	MPI-ESM-P	Germany	850-1850	1.84	1.84
NCAR	CCSM4	USA	850-1850	0.94	1.25

LM = Last Millennium experiment

Extended Data Fig. 10 | Summary of CMIP5 models from which monthly mean data were used in the last millennium analysis.